Article

Effects of Particle Diameter and Inlet Flow Rate on Gas−Solid Flow Patterns of Fluidized Bed

Zhenjiang Zhao, Ling Zhou,* Ling Bai, Wanning Lv, and Ramesh K Agarwal

Read Online

ACCESS | Metrics & More | Article Recommendations

ABSTRACT: The complex multiscale characteristics of particle flow are notoriously difficult to predict. In this study, the evolution process of bubbles and the variation of bed height were investigated by conducting high-speed photographic experiments to verify the reliability of numerical simulations. The gas−solid flow characteristics of bubbling fluidized beds with different particle diameters and inlet flow rates were systematically investigated by coupling computational fluid dynamics (CFD) and discrete element method (DEM). The results show that the fluidization in the fluidized bed will change from bubbling fluidization to turbulent fluidization and finally to slugging fluidization, and the conversion process is related to the particle diameter and inlet flow rate. The characteristic peak is positively correlated with the inlet flow rate, but the frequency corresponding to the characteristic peak is constant. The time required for the Lacey mixing index (LMI) to reach 0.75 decreases with increasing inlet flow rate; at the same diameter, the inlet flow rate is positively correlated with the peak of the average transient velocity; and as the diameter increases, the distribution of the average transient velocity curve changes from "M" to linear. The results of the study can provide theoretical guidance for particle flow characteristics in biomass fluidized beds.
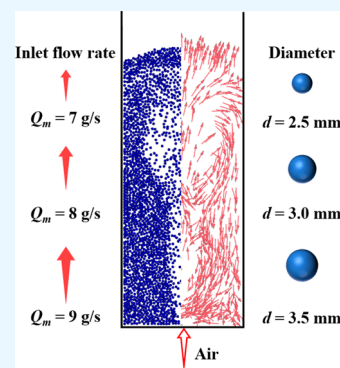
1. INTRODUCTION

As energy usage increases, interest in developing renewable energy sources has been sparked.[1] Biomass is a kind of renewable energy, which is abundant in reserves, widely distributed, and pollution-free in the world. Therefore, it is widely used as a heat source and power source, and as a substitute for fossil fuels, it has made a significant contribution to global energy production.[2] The conversion of biomass energy is a multiscale, multiphysical, and complex process, and the yield and performance of different biomass depend on the chemical composition of the molecules, physical parameters of the particles, and operating parameters of the reactor.[3−5] Since a fluidized bed has the advantages of high heat and mass transfer efficiency, wide fuel adaptability, high mixing characteristics, and there are many successful cases of biomass fluidized bed energy conversion at both the laboratory and industrial scales, it is widely used in various fields, such as biopreparation, chemical, oil exploitation, and biomass reaction.[6,7] However, the particle flow characteristics inside the bubbling fluidized bed are complex and widely used, so it has been a hot spot for research.[8,9]

On the basis of the increasing maturity of computer technology, computational fluid dynamics (CFD) has also been developed rapidly, and numerical simulation is becoming the main tool to study the particle flow characteristics and flow field distribution in fluidized beds. Currently, there are two main numerical calculation methods for gas−solid flow that are most widely used. One method is the two-fluid model (TFM),

which uses the Euler−Euler method[10] and treats the fluid and the particle population as a continuous medium and pseudocontinuous medium, respectively; the other method is the discrete element method (DEM) based on the Euler−Lagrange method.[11−13] In CFD−DEM, the gas phase is solved using Navier−Stokes equations and is regarded as the continuous phase; the particle motion is solved using Newton's second law and is regarded as the discrete phase. The method tracks each particle in the system independently and takes into account the interaction between the particles, the fluid, and the walls.[14,15] In addition, the simulation of gas−solid flow can be divided into traditional one-way coupling (considering only the action of fluid phase on solid phase), two-way coupling (considering the interaction of fluid phase and solid phases), three-way coupling (considering the effect of particle trails on subsequent particles), and four-way coupling (considering two-phase interaction while also considering solid-phase particle−particle and particle−wall collisions). The four-way coupling has been successfully used in many applications and is gradually becoming the current research frontier and research
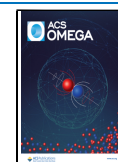
hotspot in the field of gas–solid two-phase flow.[16−18] The difficulty in the four-way coupling method is how to accurately solve the particle–particle and particle–wall collisions. Random collision model is the most effective method at present, and its accuracy has been widely recognized in the numerical calculation of fluidized bed gas–solid flow.[19]

Tsuji et al.[20] used DEM modeling to take the gas–particle interaction into account, and the flow field characteristics of the gas phase and particle motion were solved simultaneously to give a realistic image of the particle motion. Balice et al.[21] used the one-way coupling DEM model to study the deposition of droplets from 5 to 22 μm on the particle surface in a gas–solid fluidized bed, and the deposition factor was calculated and fitted to an empirical equation, which applies to the inertial region. Zhou et al.[22] used a combination of DEM four-way coupling and high-speed photographic experiments for systematic analysis of particle physical parameters on the flow process inside the fluidized bed, and the results showed that the particle diameter showed a negative correlation with the maximum value of the bed height. Chen et al.[23] discussed six different morphologies of fluidized beds on the basis of experimental studies with columnar particles, derived a theoretical model for the terminal velocity of columnar particles, and performed experimental validation. Tang et al.[24] conducted a DEM numerical simulation study on the flow behavior of single- and multinozzle fluidized beds. In comparison of the circulation rate and collision characteristics of a single-nozzle fluidized bed with a multinozzle fluidized bed, the particles were found to be better mixed in the dual-nozzle fluidized bed. Zhang et al.[25] investigated the drag coefficient, as well as the mixing characteristics, of polydisperse particles in a bubbling fluidized bed by the DEM method and analyzed the minimum fluidization velocity of four drag models. Fluidized bed hydrodynamic properties significantly affect the particle fluidization behavior within the bed and, thus, the overall performance of the fluidized bed. In addition to bed size, the gas temperature; pressure and velocity; and operating conditions, such as particle size and particle shapes, have significant effects on bed fluid dynamics.[26−29] Therefore, an in-depth understanding of the operating parameters is of great importance for the flow characteristics of fluidized beds and the distribution of the internal flow field.

In this work, the CFD−DEM four-way coupling method is used to analyze the flow characteristics inside the bubbling fluidized bed and the gas-phase flow field distribution. The overall plan of this work is as follows. The controlling equations of fluid flow and mass motion are given in Section 2. The experimental details and the validation of the CFD−DEM method is stated in Section 3, and the reliability of the numerical simulations by high-speed photographic experiments is evaluated. In Section 4 the influence of particle diameter and inlet flow rate on the fluidization evolution process, mixing characteristics, and axial velocity of the fluidized bed is investigated. The main conclusions are given in Section 5.

2. SIMULATION METHOD

2.1. Gas Phase.
The gas phase flow field is solved by the locally volume-averaged Navier−Stokes equations. The equation is described in detail in other literature and will not be repeated here.[30,31]

The main equations include the mass conservation equation

$$\frac{\partial \varepsilon \rho_f}{\partial t} + \nabla(\varepsilon \boldsymbol{u}_f) = 0 \tag{1}$$

and momentum conservation equation

$$\frac{\partial(\varepsilon \rho_f \boldsymbol{u}_f)}{\partial t} + \nabla(\varepsilon \boldsymbol{u}_f \boldsymbol{u}_f) = -\varepsilon \nabla P + \nabla(\varepsilon \boldsymbol{\tau}_f) + \varepsilon \rho_f \boldsymbol{g} + \boldsymbol{F}_{pf} \tag{2}$$

where ε is the porosity, ρ_f is the gas fluid, $\boldsymbol{u}_f$ is the gas velocity vector, P is the shared pressure, and $\boldsymbol{\tau}_f$ is the molecular viscous stress tensor of the gas phase, which is defined as

$$\boldsymbol{\tau}_f = \mu_f(\nabla \boldsymbol{u}_f + \nabla \boldsymbol{u}_f^T) + \left(\lambda_f - \frac{2}{3}\mu_f\right)\nabla \times u_f I \tag{3}$$

where $\boldsymbol{F}_{pf}$ is the momentum source term that is generated as a result of the interaction between the two phases:

$$\boldsymbol{F}_{pf} = -\frac{\sum_{p=1}^{N_{grid}} \boldsymbol{F}_{fp}}{V_{grid}} \tag{4}$$

where V_{grid} and N_{grid} are the volume of the CFD grid and number of particles located in the local grid, respectively. $\boldsymbol{F}_{pf}$ is the force exerted on the particle by the fluid.

2.2. Solid Phase.
For solid-phase particles, the particle motions (translational motion and rotational motion) are solved by the first and second laws of the explicit Euler method, respectively, to track every particle in the fluidized bed by the Lagrangian method:[32−34]

$$m_p \frac{d\boldsymbol{v}_p}{dt} = \boldsymbol{F}_c + \boldsymbol{F}_{fp} + m_p \boldsymbol{g}$$

$$= \boldsymbol{F}_c + \boldsymbol{F}_d + \boldsymbol{F}_{\nabla p} + \boldsymbol{F}_L + \boldsymbol{F}_V + \boldsymbol{F}_{others} + m_p \boldsymbol{g} \tag{5}$$

$$J_p \frac{d\boldsymbol{\omega}_p}{dt} = \boldsymbol{M}_c + \boldsymbol{M}_{fp} \tag{6}$$

where m_p is the particle mass, g is the gravitational acceleration vector, $\boldsymbol{F}_c$ is the contact force that accounts for particle–particle and particle–wall collisions, $\boldsymbol{\omega}_p$ is the angular velocity vector, J_p is its moment of inertia, and $\boldsymbol{M}_c$ is the net torque generated by tangential forces that causes the rotation of the particle. $\boldsymbol{F}_{fp}$ is the fluid interaction force. It usually consists of the drag force ($\boldsymbol{F}_d$), the pressure gradient force ($\boldsymbol{F}_{\nabla p}$), the virtual mass force ($\boldsymbol{F}_V$), the lift force ($\boldsymbol{F}_L$), and the other force ($\boldsymbol{F}_{others}$). The drag force $\boldsymbol{F}_d$ is definite:

$$\boldsymbol{F}_d = \frac{1}{2} C_D \rho_f A' |\boldsymbol{u} - \boldsymbol{v}_p|(\boldsymbol{u} - \boldsymbol{v}_p) \tag{7}$$

where $\boldsymbol{u} - \boldsymbol{v}_p$ is the relative velocity between particle and fluid, A' is the projected particle area in the flow direction, and C_D is the drag coefficient.

In the DEM numerical simulation, it is assumed that the particles are spheres with certain elasticity, which are allowed to produce certain elastic deformation when the collision occurs, and the force during the collision is calculated by this deformation variable. Based on the soft sphere model, the forces on the particles during the collision are calculated on the basis of the most widely used elastic-damper model, which contains the Hooke elastic model as well as the Newtonian damper model, and the elastic deformation during the collision is calculated by the Hooke elastic model, while the inelastic deformation is calculated by the Newtonian damper model.

Figure 1 shows particle i, the particle j with position vectors $\boldsymbol{x}_i$, $\boldsymbol{x}_j$, and radii R_i and R_j, which are in physical contact.[35]

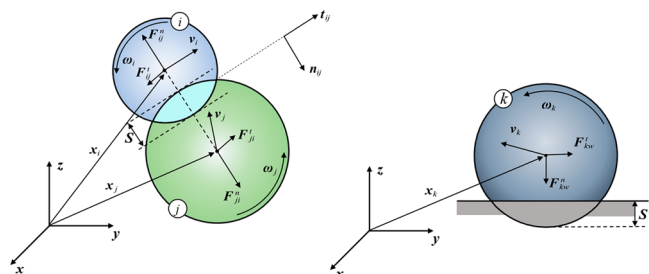$$S_n = R_i + R_j - |x_j - x_i| \tag{8}$$

Figure 1. Schematic diagram of the concept after interparticle collisions and particle−wall collisions.

When collisions occur between particles, the collision force between the particles can be decomposed into normal collision force and tangential collision force.[36]

$$\boldsymbol{F}_{ij}^{co} = \boldsymbol{F}_{ij}^n + \boldsymbol{F}_{ij}^t \tag{9}$$

The relative velocity of the particle at the collision point:

$$\boldsymbol{v}_{ij} = \boldsymbol{v}_i - \boldsymbol{v}_j + (R_i\boldsymbol{\omega}_i + R_j\boldsymbol{\omega}_j) \times \boldsymbol{n}_{ij} \tag{10}$$

The normal velocity component at the point of collision:

$$\boldsymbol{v}_{ij}^n = (\boldsymbol{v}_{ij} \times \boldsymbol{n}_{ij})\boldsymbol{n}_{ij} \tag{11}$$

The tangential velocity component at the point of collision:

$$\boldsymbol{v}_{ij}^t = \boldsymbol{v}_{ij} - \boldsymbol{v}_{ij}^n \tag{12}$$

The normal vector is defined as

$$\boldsymbol{n}_{ij} = \frac{\boldsymbol{x}_j - \boldsymbol{x}_i}{|\boldsymbol{x}_j - \boldsymbol{x}_i|} \tag{13}$$

Having the tangential velocity at contact point, the tangential overlap is then calculated as

$$\boldsymbol{t}_{ij} = \frac{\boldsymbol{v}_{ij}^t}{|\boldsymbol{v}_{ij}^t|} \tag{14}$$

3. EXPERIMENTAL AND SIMULATION SETUP

3.1. Experimental Procedure. In order to study the flow characteristics of particles in fluidized beds under different conditions (particle diameter, inlet flow rate) and the flow field distribution of the gas phase, high-speed photographic experiments were carried out in this work. Plexiglas was allowed to be used as the fabrication material for the fluidized bed (for specific dimensions, see Section 3.2). Glass balls are used as the material of the particles in the experiment, which have the advantages of high mechanical strength and good wear resistance. First, the number of particles required for the experiment is prepared, and the required particles are weighed out by unit conversion and by a precision electronic balance. Then, the lines are connected in order according to the process shown in Figure 2. In order to eliminate the moisture in the gas flowing through the refrigerated dryer to ensure the stability of the injected air pressure, the air compressor and refrigerated dryer are turned on 15 min in advance. Next, the weighed
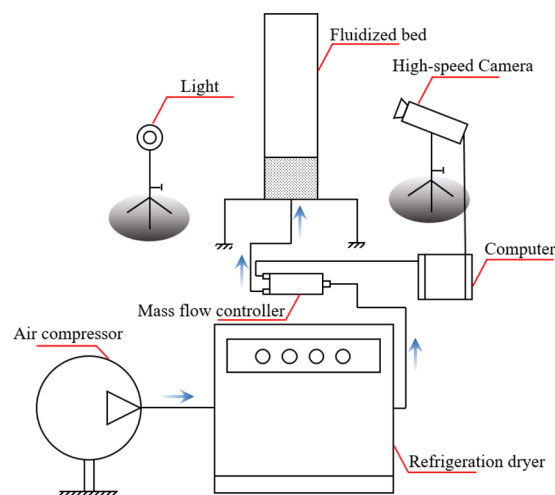

Figure 2. Schematic diagram of the experiment.

particles are slowly poured in from the top of the fluidized bed, and the top of the bed is stirred with a fine iron rod to make it flat. The exit of the fluidized bed is blocked by a fine screen to prevent the particles from flying out. Finally, the fill light is turned on, and the intensity of the light source is adjusted, while the height of the high-speed camera (1000 frames per second was used in this experiment); the distance from the fluidized bed, to minimize the ghosting of the particles and improve the clarity of the image; and control of the flow rate of the gas injected into the fluidized bed through the computer window after completing the above work are appropriately adjusted. It is worth noting that after completing one experiment, the interval between two experiments was greater than 5 min to eliminate the effects caused by static electricity in the fluidized bed.

3.2. Computational Model and Simulation Conditions. The geometric model of the fluidized bed used in this work has a height of 1000 mm, a width of 20 mm, and a length of 150 mm, and the origin of the coordinates is located at the center of the inlet A. It is worth noting that the inlet is made of nine evenly distributed circular holes, which are intended to prevent particles from falling off when at rest. In addition, the diameter of the circular holes is 2 mm, but in the numerical simulation, in order to improve the mesh quality and speed up the convergence time, the inlet uses rectangular holes with the same area as the experimental area, and the size of the rectangular inlet is 5.6 mm × 5 mm, as shown in detail in Figure 3.

In CFD, "mass flow inlet" and "pressure outlet" are the entrance boundary condition and the outlet boundary condition, respectively. The standard k-ε turbulence model is used to describe the effect of turbulence on the flow, and "Phase Couples SIMPLE" is regarded as the pressure−velocity coupling. "Huilin and Gidazpow" is chosen for the drag model in the DEM, and volumetric diffusion is used as the mapping method. The standard wall function is used for near-wall treatment. The detailed calculation parameters are shown in Table 1.

3.3. Grid Independence Analysis and Simulation Reliability Verification. In this paper, ANSYS ICEM software is used to divide the computational domain of the gas−solid fluidized bed into different numbers of grids, which are 1.48×10^4, 3.06×10^4, 3.49×10^4, 3.93×10^4, 4.40×10^4, 5.45×10^4. In the simulation for different grid numbers, P_1(0,
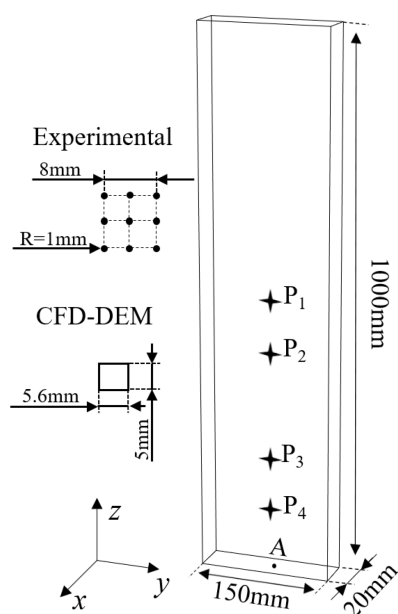
Figure 3. Geometry of fluidized bed and grid division.

Table 1. Calculation Parameters

parameter	value	unit
gas density (ρ_g)	1.25	kg/m³
gas viscosity (μ_g)	1.8×10^{-6}	Pa·s
solid density (ρ_s)	2500	kg/m³
gas phase time step (t_{CFD})	1×10^{-4}	s
particle phase time step (t_{DEM})	9.5×10^{-7}	s
coefficient of restitution (e)	0.9	
static friction coefficient (μ_s)	0.3	
dynamic friction coefficient (μ_s)	0.3	

0, 500), P_2(0, 0, 400), and P_3(0, 0, 200) are selected as pressure monitoring points. Figure 4 shows the pressure difference between P_1 and P_2 and between P_1 and P_3. It can be obtained that when the grid number is encrypted to 3.06×10^4, the pressure difference curve fluctuates very little. At the same time, in the DEM of the Lagrangian system, the grid size should be at least 1.63 times the particle diameter.[37] Otherwise, the void rate in a single grid will be "singularity,"
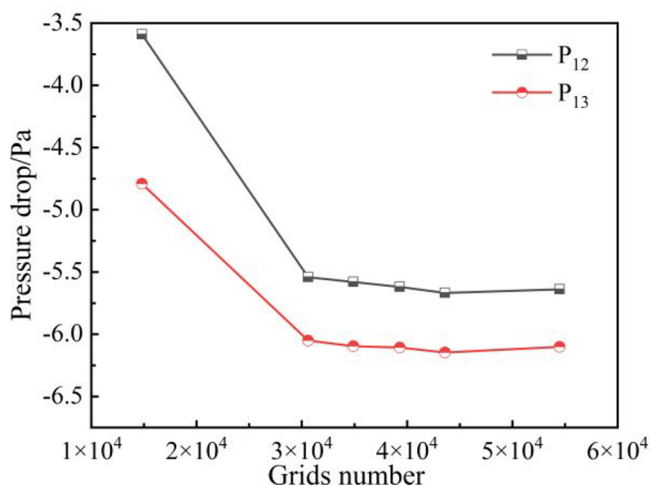

Figure 4. Grid independence verification.

which easily causes convergence errors. Therefore this work uses a grid number of 3.06×10^4 to obtain calculation results that match the actual ones and save computational resources. The calculation grid size is greater than 3 times the maximum size of the particle for this simulation, which satisfies the requirement.

Under the same conditions (inlet flow rate of 7 g/s and particle number of 30 000), the bed height is compared between numerical simulation and experiment at different moments with the aim of verifying the reliability of the CFD−DEM coupling used in this work. Figure 5 shows the evolution of the fluidized bed over time under high-speed photography experiments and numerical calculation. What can be obtained is that both experiments and simulations can capture the classical bubble morphology and describe the behavior of the falling process of the particles by both methods consistently after the bubble breakup at 540 ms. Additionally, a C-shaped bubble appears on both sides at the top of the experiment and the simulation at 720 ms.

In addition, it can be seen from Figure 6 that the maximum error of the bed height occurs at 180 ms with a value of 4.82%, and the bed height obtained from the experiments and numerical simulations are in good agreement, which indicates the reliability of the numerical simulations.

4. RESULTS AND DISCUSSION

To reveal the evolutionary mechanisms within gas−solid fluidized beds under different conditions, nine different cases (shown in Table 2) were developed in this work on the basis of conventional CFD−DEM coupling calculations to analyze the void fraction, solid phase translation velocity, axial velocity, absolute velocity, and LMI.

4.1. Void Fraction. The evolution of the gas phase flow field inside the fluidized bed is indirectly derived by comparing the distribution of void fraction inside the fluidized bed at different inlet flow rates. Figure 7 shows the transient distribution of void fraction of the fluidized process in the fluidized bed at different inlet flow rates. At the initial moment, the numerically simulated particles in the three operating conditions are closely aligned at the bottom of the bed, at a stationary state, and with zero initial kinetic energy. Before 0.3 s, as the gas is injected into the fluidized bed, the closely packed bed of particles begins to expand and gradually increase in height because of the lifting effect of the airflow, and elliptical bubbles are gradually formed inside with the particles at the top of the bubble having a higher velocity while the particles on the lower sides of the bubble are caught in the bubble because of the existence of the "entrainment effect." At 0.3−0.7 s, with the continuous injection of gas, the bed continues to expand, the internal bubble area gradually becomes larger, the ellipse gradually becomes rectangular, and the single bubble becomes multiple bubbles. However, the number of particles at the top of the bubble gradually becomes fewer, and the bubble starts to rupture, at which time the particle flow state in the fluidized bed changes from the original bubbling flow state to the turbulent flow state. At 0.7−1 s, the bubble is completely ruptured, and the particles start to fall along the wall to the bed while some other particles fall to the inlet because of gravity. Between 1−6 s, although the gas continues doing work on the particles, the change of bed height is not obvious, and a new bubble appears at the inlet of the bed, thereby forming a solid phase back-mixing phenomenon.[38] At the start-up phase where the bubble area
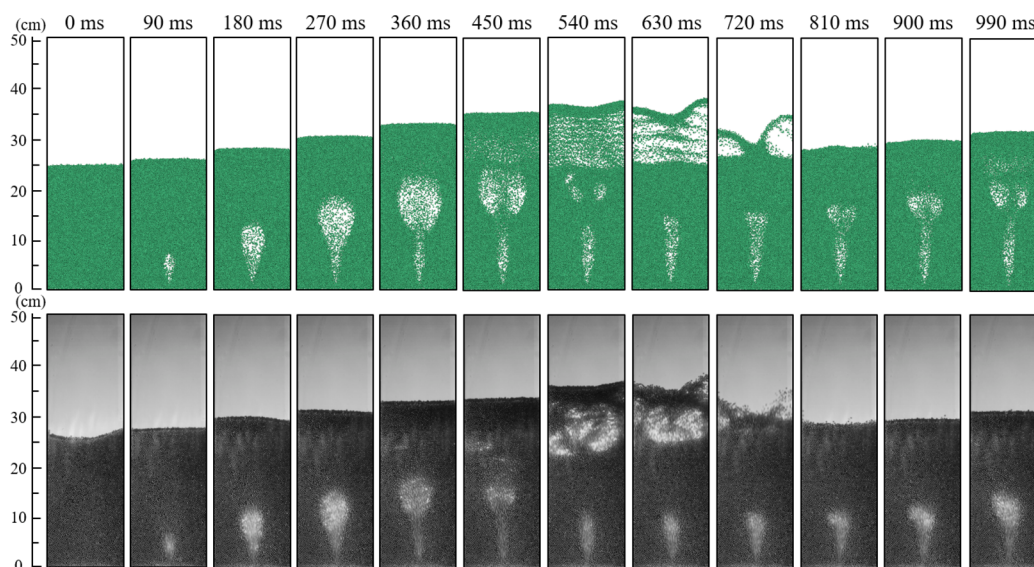
Figure 5. Snapshot comparison at different moments, d = 3.0 mm, Q_m = 7 g/s.
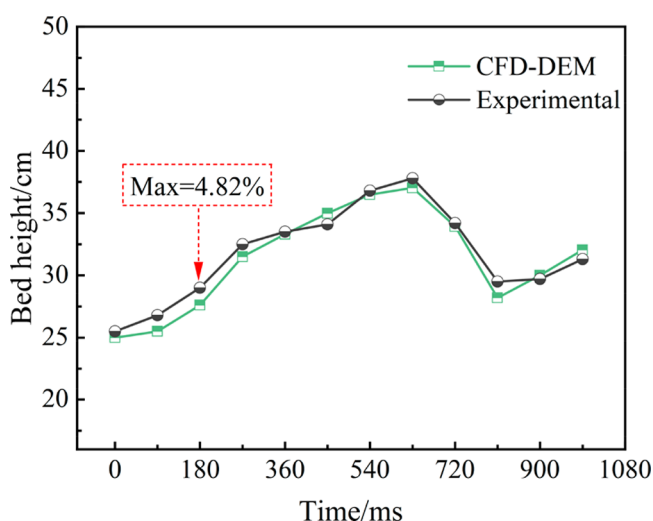

Figure 6. Comparison of bed height between CFD−DEM and experiment.

Table 2. Calculation Scheme of Different Inlet Flow Rates

inlet flow rate/(g/s)	particle diameter/mm	number of particles
7	2.5	52 152
	3.0	30 000
	3.5	18 684
8	2.5	52 152
	3.0	30 000
	3.5	18 684
9	2.5	52 152
	3.0	30 000
	3.5	18 684

is smaller, the upper particles at the entrance are closely stacked, and the gas does work to the overall bed of particles, but after 1 s, because the upper particles at the entrance become loosely stacked, the gap between the particles becomes larger, and the gas does much more work to the particles within the black dashed box of Figure 7a than the other particles, which causes the top particle layer bubble in the

formation to be very thin. Because this phase does not occur in the start-up phase fluidization behavior, it is at this time that the flow regime in the particle bed changes from the original turbulent fluidization to slugging fluidization. In addition, after 1, 4, and 6 s in Figure 7a and after 3 and 5 s in Figure 7c, the same bubble shape is captured, and the particle−particle collisions will be more severe than in the start-up phase.[39] It is worth noting that the inlet flow rate exerts a large influence on the bed height and bubble diameter. Especially at the initial stage, the bubble area, the bed height, and the time required to enter the slugging fluidization are positively correlated with the inlet flow rate.

To further investigate the effect of particle diameter on fluidization behavior in gas−solid fluidized beds, particles of 3.5 mm were selected to analyze the evolution of gas−solid transient flow in fluidized beds. Figure 8 shows the transient distribution of the void fraction of the fluidization process in the fluidized bed with different inlet gas flow rates. What can be observed is that the fluidized bed evolution process also goes through bubble generation, rupture, and then enters the steady cycle state when using 3.5 mm diameter particles. Additionally, the bubble area and bed height become larger with the increase of the inlet flow rate. By looking at Figure 8a and Figure 7a, it can be summarized that at the inlet flow rate of 7 g/s, the 3.5 mm granular bed bubble effect is poor, the bed height does not change much, and turbulent fluidization and slugging fluidization do not occur, which is a big difference from the flow phenomenon in the 2.5 mm granular bed. In addition, from Figure 8 a, it can be seen that an oscillatory stratification phenomenon appears in the gas phase distribution at 0.8 and 0.9 s at the top of the bed particles. When using 8 g/s as the inlet flow rate, the oscillatory stratification disappears, and turbulent fluidization occurs. When the inlet flow rate continues to increase to 9 g/s, the fluidization in the fluidized bed starts to change from bubbling fluidization to turbulent fluidization to slugging fluidization, which is consistent with the conclusion of Han et al.[40] In summary of the above, it is concluded that the larger the particle diameter, the more energy is required to drive the particles to the fluidized state and the larger of an inlet flow rate is required. Therefore, the flow characteristics inside the fluidized bed are
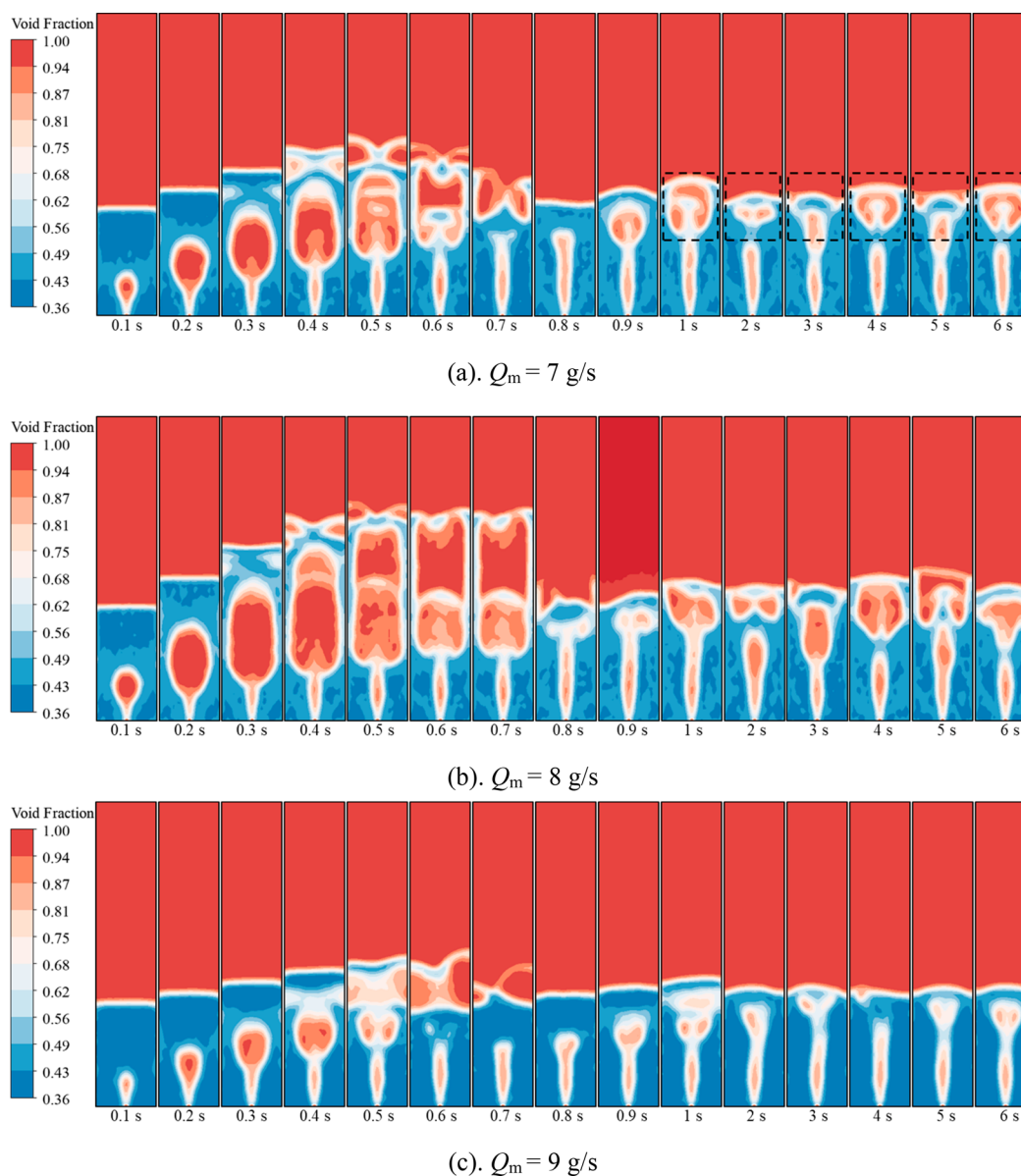
(a). $Q_m = 7$ g/s

(b). $Q_m = 8$ g/s

(c). $Q_m = 9$ g/s

Figure 7. Snapshot of void fraction of numerical simulation, $d = 2.5$ mm.

very sensitive to the inlet flow rate and particle size, and it is necessary to study them in more detail.

4.2. Solid-Phase Translation Velocity. Figure 9 shows the translational velocity vectors of the $x = 0$ cross section of the fluidized bed. Before 0.3 s, with the entry of gas, the particle vector is upward as a whole, and the upper particle vectors on both sides of the bubble point upward and toward the wall, respectively, while the lower ones point toward the inlet (as shown by the red arrows); between 0.3 and 0.35 s, the particle population at the top of the bed begins to stratify (as shown by the red dashed box), and the particle vectors appear in opposite directions.

Between 0.4 and 0.6 s, the particles on both sides of the air bubble inside the particle bed move downward and more closely to the wall, the vector direction turns downward, the collision of particles inside the bubble intensifies, the vector direction points around, the particles at the top start to fall, and then C-shaped bubbles appear on both sides at the top of the particles, which is consistent with the results in Figure 8. At 0.55 s, we can see clearly that two small bubbles appear inside

the large bubble, which are located on both sides of the entrance, and it can be seen in Figure 9 that they have been formed at 0.6 s. With the formation of double bubbles inside, the height of the large bubble gradually decreases before the rupture occurs at 0.6 s. Until 0.8 s, the particles at the top of the bubble descend to the bed, and the large bubble disappears completely. After 0.9 s, small bubbles are stably formed, and the bed height changes less. In short, the particle flow characteristics are characterized by high void fraction in the bubble area, but large particle velocity and upward direction, or low void fraction at both sides of the wall with downward movement, which in turn forms a single bubble flow pattern.

4.3. Axial Velocity. The particle motion process within the fluidized bed was investigated by varying the particle diameter and the inlet flow rate. The variation of the axial velocity of the particles in the local region on the time scale was tracked in the numerical simulation. The center point of the local region is $P_4(0, 0, 122)$ with a statistical size of $20(x) \times 150(y) \times 5(z)$. Figure 10 shows the relationship between the average axial velocity of particles in the local area with time for the three
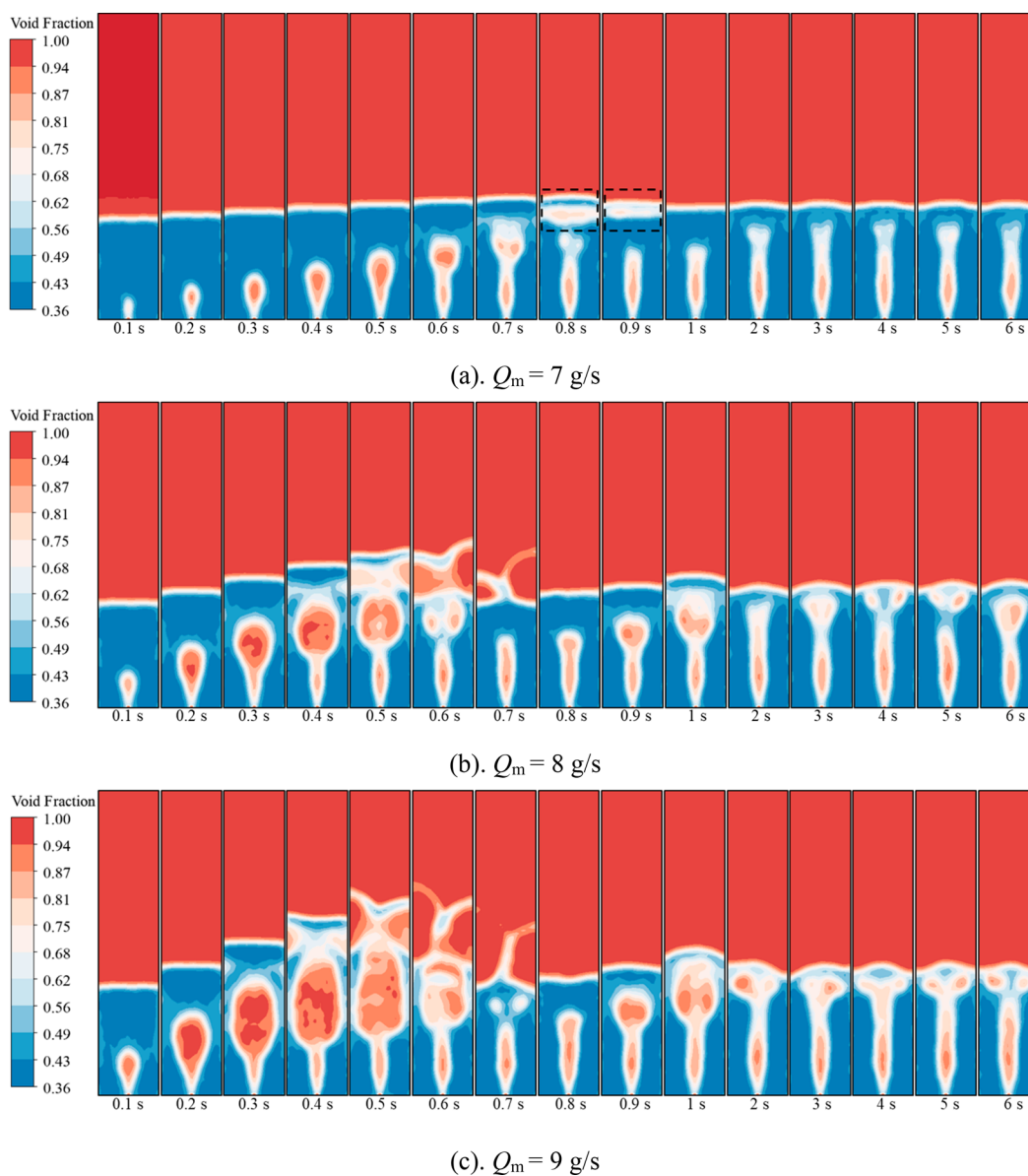
(a). Q_m = 7 g/s

(b). Q_m = 8 g/s

(c). Q_m = 9 g/s

Figure 8. Snapshot of void fraction of numerical simulation, d = 3.5 mm.

particle sizes at different inlet flow rate conditions. It can be seen that the average axial velocity under each case has obvious fluctuation cases. When using particles with a diameter of 2.5 mm, the time series of the average axial velocity in each case has a certain regular fluctuation, and the fluctuation magnitude shows a positive correlation with the inlet flow rate because the larger inlet flow rate leads to a greater force of gas on the particles, and the collision force becomes the main contact form between the particles. When using particles with a diameter of 3.0 mm, the curves under the latter two cases also show regular fluctuations, but the time series of particle velocity at 7 g/s basically has no obvious regular fluctuations. However, as the particle diameter increases, the fluctuations of particle axial velocity with time under the three cases are more chaotic, and there is no obvious periodic fluctuation, which is because of the fact that as particle size increases, the particles are subjected to a gradually decreasing axial force. This leads to the change of particle contact form from collision force to shear force.

To quantitatively study the fluctuation characteristics of the mean axial velocity of the particles, the time series of the mean axial velocity for each case was subjected to fast Fourier transform, and Figure 11 shows the obtained spectrum. Figure 11a shows the spectrum of the particle size, which is 2.5 mm in the three cases, and it is obvious that the spectrum shows an obvious characteristic peak; the frequency of the characteristic peak in the different cases is about 4.5 Hz, and the amplitude increases with the increase of the inlet flow rate, which is more similar to the velocity fluctuation amplitude in Figure 10a. It should be noted that the frequency of the characteristic peak is about 4.1 Hz at 8 and 9 g/s in Figure 11b, whereas at the inlet flow rate of 7 g/s, the peaks of the spectrum are more haphazard, and no obvious dominant characteristic peak can be seen. The spectrograms in Figure 11c all show the characteristic peaks. Combining Figure 10 and Figure 11, it is noticeable that the particle axial velocity in each case shows obvious fluctuation characteristics; at the same inlet flow rate, the fluctuation characteristics gradually strengthen as the particle diameter decreases; at the same particle diameter, the
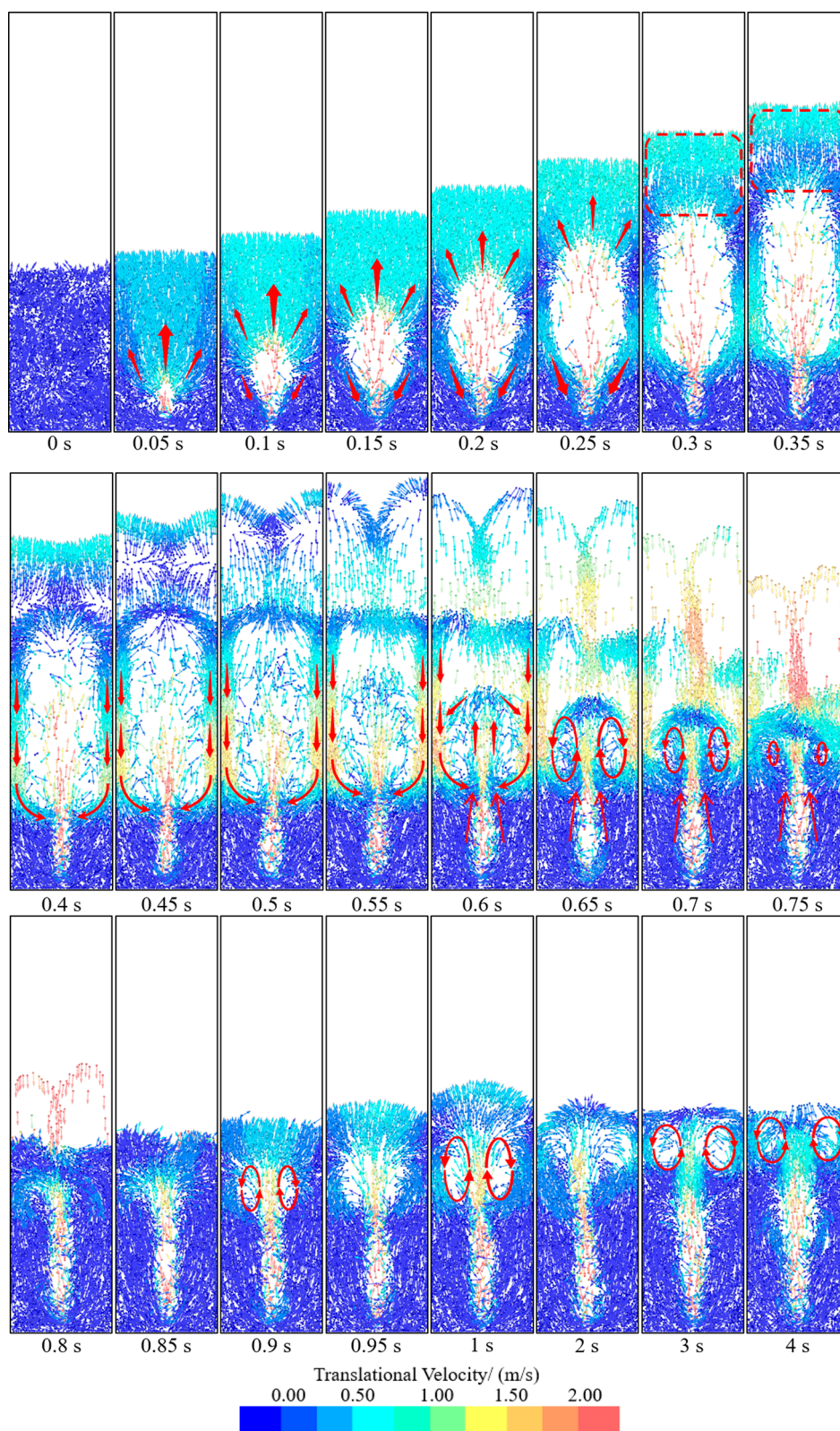
Figure 9. Velocity vector distribution of solid particles; d = 3.0 mm, Q_m = 9 g/s.

fluctuation characteristics gradually weaken as the inlet flow rate decreases.

4.4. Absolute Velocity. Figure 12 show the average of the norm sum of all particle transient velocity vectors at different conditions (Q = 7, 8, or 9 g/s; d = 2.5, 3.0, or 3.5 mm)

From Figure 12a, the average transient velocity curve shows an "M" shape at the diameter of 2.5 mm, and the curve shifts upward with an increase of the inlet flow rate as a whole. At the inlet flow rate of 7 g/s, the average transient velocity curve distribution gradually changes from an "M" shape to
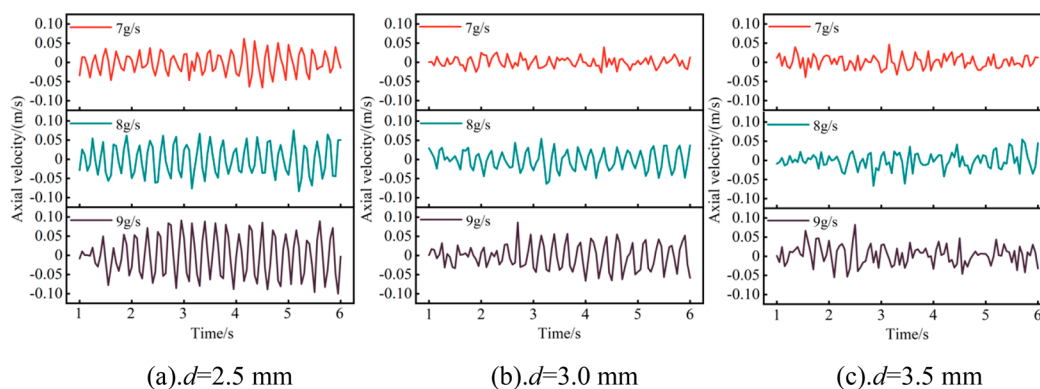
Figure 10. Average axial velocity of particles at different inlet flow rates.
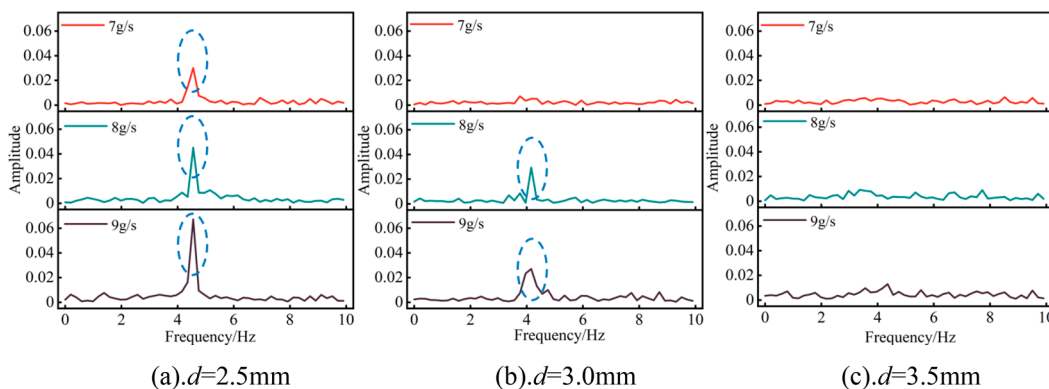

Figure 11. Fourier spectrum of the time series of the mean axial velocity of particles.
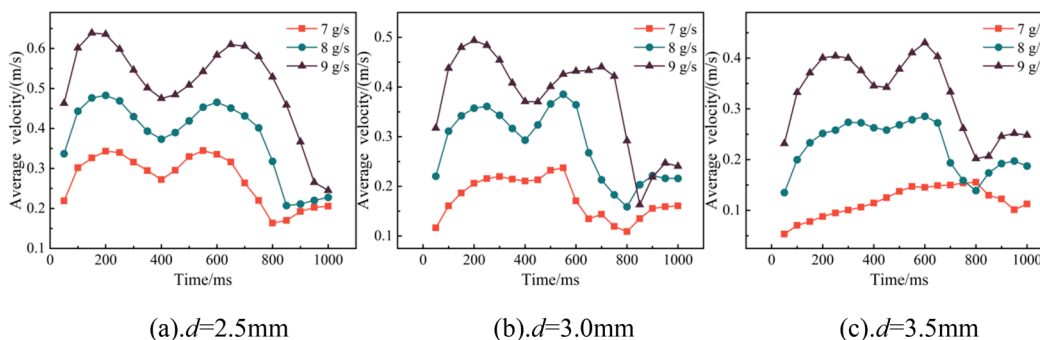

Figure 12. Average velocity of particles at different inlet flow rates.

approximately linear as the particle diameter increases; when the inlet flow rate is 8 g/s, the average transient velocity curve distribution remains "M"-shaped for the 2.5 and 3.0 mm particle beds, while the average transient velocity curve for the 3.5 mm particle beds becomes approximately semicircular in distribution. At the inlet flow rate of 9 g/s, the average transient velocity curve for all three particle diameters becomes "M"-shaped.

4.5. Mixed Characteristics. It is challenging to analyze the degree of mixing of particles inside the bed at the macroscopic scale. The Lacey Mixing Index (LMI) can quantify the degree of mixing: an index of 0 means complete segregation, an index of 1.0 means complete random mixing, and an index between 0.75 and 1.0 means a "good" mix. Therefore, LMI is introduced to quantitatively analyze the particle mixing degree in this paper.[32,41]

$$\text{LMI} = \frac{S^2 - S_0^2}{S_R^2 - S_0^2} \tag{15}$$

where S^2 is the mass fraction variance, S_0^2 is the variance of a fully segregated system, and S_R^2 is the variance of fully mixed system. In the calculation of the LMI, the precalculated area is classified into a certain number of samples. Because the particles are constantly moving in the fluidized bed, the number of particles in each sample may vary greatly. To minimize the error, a weighting method is used to solve this problem.

$$S^2 = \frac{1}{N-1}(w_i - \overline{w})^2 \tag{16}$$

where N is the number of cells, w_i is the tracer particles mass fraction in the cell i, and $\overline{w}$ is the average tracer particles mass fraction across cells.
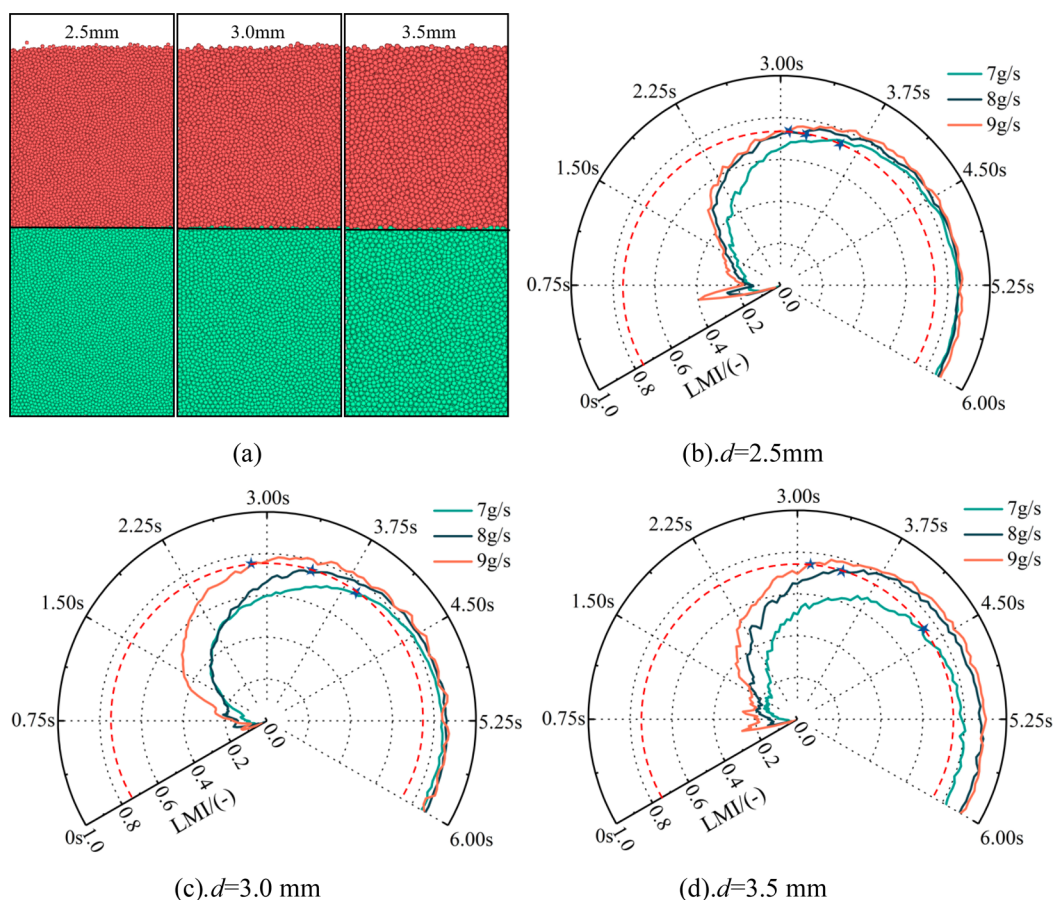
Figure 13. Relationship between LMI at different times.

The green particles in Figure 13a were selected as tracer particles, while the fluidized bed was divided into 15 × 4 × 100 cells for sampling by Eulerian statistics, and the variation patterns of LMI for three particle diameters (d = 2.5, 3.0, and 3.5 mm) at three inlet flow rates were investigated. The results are shown in Figure 13. It can be seen that the LMI is above 0.75 for each case at t = 6 s. When the inlet flow rate is 7 and 8 g/s, the time required to reach an LMI of 0.75 shows a positive correlation with the particle diameter (the red dashed line in the figure shows LMI = 0.75). In addition, the inlet flow rate shows a negative correlation with the time required for "good" mixing at the same particle diameter, but the time interval is positively correlated with the larger particle diameter.

5. CONCLUSION

In this work, the flow characteristics of the bubbling fluidized bed were systematically analyzed on the basis of a combination of CFD−DEM four-way coupling and high-speed photographic experiments, from which the following conclusions have been obtained.

Through analysis of the distribution of the void fraction at different moments, the influence of inlet flow rate and particle diameter on the bed height and bubble diameter is very obvious, which shows that the bed height and bubble area increase with the increase of inlet flow rate under the same time node. With time, the bubble fluidizes the bed fluidization from bubble fluidization to turbulent fluidization and finally to slugging fluidization. However, when 3.5 mm diameter particles with an inlet flow rate of 7 g/s are used, the bubble effect is poor, and the fluidization transitions directly from

bubble fluidization to slugging fluidization. It indicates that the energy required to drive the larger diameter particles to reach the fluidization state is positively correlated with the inlet flow rate. It is concluded from analysis of the solid-phase vector distribution of particles with a diameter of 3.0 mm and an inlet flow rate of 9 g/s that the final flow mode of the bubbling fluidized bed is transformed from a single bubble to a double bubble.

The average axial velocity showed obvious regular fluctuations in the time series, and the amplitude of fluctuations was positively correlated with the inlet flow rate, but irregular fluctuations occurred in the average axial velocity curve at the particle diameter of 3.5 mm. The frequency of the characteristic peak shows a negative correlation with the particle diameter, and the amplitude at each particle diameter decreases with the increase of the inlet flow rate. When the inlet flow rate is 9 g/s, the average transient velocity distribution of the particle bed at all three particle diameters is "M"-shaped. The time required for the LMI to reach above 0.75 was positively correlated with particle diameter and inlet flow rate, and the LMI was maximized at a particle diameter of 3.5 mm and inlet flow rate of 9 g/s with a value of 0.91.

■ AUTHOR INFORMATION

Corresponding Author

    Ling Zhou − *Research Center of Fluid Machinery Engineering and Technology, Jiangsu University, Zhenjiang 212013, China;* ⊙ orcid.org/0000-0001-9868-2561; Phone: 86-13815477737; Email: lingzhou@ujs.edu.cn

Authors

Zhenjiang Zhao − *Research Center of Fluid Machinery Engineering and Technology, Jiangsu University, Zhenjiang 212013, China*

Ling Bai − *Research Center of Fluid Machinery Engineering and Technology, Jiangsu University, Zhenjiang 212013, China*

Wanning Lv − *Research Center of Fluid Machinery Engineering and Technology, Jiangsu University, Zhenjiang 212013, China*

Ramesh K Agarwal − *Department of Mechanical Engineering and Materials Science, Washington University in St. Louis, St. Louis, Missouri 63130, United States;* ⓘ orcid.org/0000-0002-9642-1023

Complete contact information is available at:
https://pubs.acs.org/10.1021/acsomega.3c00118

Notes

The authors declare no competing financial interest.

■ REFERENCES

(1) Roy, M. M.; Dutta, A.; Corscadden, K.; Havard, P.; Dickie, L. Review of biosolids management options and co-incineration of a biosolid-derived fuel. *Waste Manag* **2011**, *31* (11), 2228−35.

(2) Thanigaivel, S.; Priya, A. K.; Dutta, K.; Rajendran, S.; Sekar, K.; Jalil, A. A.; Soto-Moscoso, M. Role of nanotechnology for the conversion of lignocellulosic biomass into biopotent energy: A biorefinery approach for waste to value-added products. *Fuel* **2022**, *322*, 124236.

(3) Carpenter, D.; Westover, T. L.; Czernik, S.; Jablonski, W. Biomass feedstocks for renewable fuel production: a review of the impacts of feedstock and pretreatment on the yield and product distribution of fast pyrolysis bio-oils and vapors. *Green Chem.* **2014**, *16* (2), 384−406.

(4) Fahmi, R.; Bridgwater, A. V.; Donnison, I.; Yates, N.; Jones, J. M. The effect of lignin and inorganic species in biomass on pyrolysis oil yields, quality and stability. *Fuel* **2008**, *87* (7), 1230−1240.

(5) Zhou, L.; Hang, J.; Bai, L.; Krzemianowski, Z.; El-Emam, M.; Yasser, E.; Agarwal, R. Application of entropy production theory for energy losses and other investigation in pumps and turbines: a review. *Applied Energy* **2022**, *318*, 119211.

(6) Cui, H.; Grace, J. R. Fluidization of biomass particles: A review of experimental multiphase flow aspects. *Chem. Eng. Sci.* **2007**, *62* (1−2), 45−55.

(7) Salatino, P.; Solimene, R. Mixing and segregation in fluidized bed thermochemical conversion of biomass. *Powder Technol.* **2017**, *316*, 29−40.

(8) Alobaid, F.; Ohlemüller, P.; Ströhle, J.; Epple, B. Extended Euler-Euler model for the simulation of a 1 MWth chemical-looping pilot plant. *Energy* **2015**, *93*, 2395−2405.

(9) Zarekar, S.; Bück, A.; Jacob, M.; Tsotsas, E. Numerical study of the hydrodynamics of fluidized beds operated under sub-atmospheric pressure. *Chemical Engineering Journal* **2019**, *372*, 1134−1153.

(10) Rauchenzauner, S.; Schneiderbauer, S. A dynamic Spatially Averaged Two-Fluid Model for heat transport in moderately dense gas-particle flows. *Phys. Fluids* **2020**, *32* (6), 063307.

(11) Lathouwers, D.; Bellan, J. Modeling of dense gas-solid reactive mixtures applied to biomass pyrolysis in a fluidized bed. *International Journal of Multiphase Flow* **2001**, *27* (12), 2155−2187.

(12) El-Emam, M. A.; Zhou, L.; Shi, W.; Han, C.; Bai, L.; Agarwal, R. Theories and Applications of CFD-DEM Coupling Approach for Granular Flow: A Review. *Archives of Computational Methods in Engineering* **2021**, *28* (7), 4979−5020.

(13) Wang, Z.; Lim, C. J.; Grace, J. R. Solids mixing in a dual-column slot-rectangular spouted bed. *Powder Technol.* **2016**, *301*, 1264−1269.

(14) Deen, N. G.; Van Sint Annaland, M.; Van der Hoef, M. A.; Kuipers, J. A. M. Review of discrete particle modeling of fluidized beds. *Chem. Eng. Sci.* **2007**, *62* (1−2), 28−44.

(15) Wang, J.; Ku, X.; Lin, J.; Yang, S. Impact of the Reactor Structure on Biomass Pyrolysis in Fluidized-Bed Reactors: A Coarse-Grained CFD-DEM Study. *Energy Fuels* **2021**, *35* (12), 10035−10050.

(16) Zhong, W.; Xiong, Y.; Yuan, Z.; Zhang, M. DEM simulation of gas-solid flow behaviors in spout-fluid bed. *Chem. Eng. Sci.* **2006**, *61* (5), 1571−1584.

(17) Zhao, P.; Xu, J.; Liu, X.; Ge, W.; Wang, J. A computational fluid dynamics-discrete element-immersed boundary method for Cartesian grid simulation of heat transfer in compressible gas-solid flow with complex geometries. *Phys. Fluids* **2020**, *32* (10), 103306.

(18) Sun, X.; Sakai, M. Three-dimensional simulation of gas-solid-liquid flows using the DEM-VOF method. *Chem. Eng. Sci.* **2015**, *134*, 531−548.

(19) Kriebitzsch, S. H. L.; van der Hoef, M. A.; Kuipers, J. A. M. Fully resolved simulation of a gas-fluidized bed: A critical test of DEM models. *Chem. Eng. Sci.* **2013**, *91*, 1−4.

(20) Tsuji, Y.; Kawaguchi, T.; Tanaka, T. Discrete particle simulation of two-dimensional fluidized bed. *Powder technology* **1993**, *77* (1), 79−87.

(21) Balice, D. M.; Molenaar, C. W. C.; Fochesato, M.; Venier, C. M.; Roghair, I.; Deen, N. G.; van Sint Annaland, M. CFD modeling of droplet permeability in fluidized beds. *International Journal of Multiphase Flow* **2022**, *152*, 104069.

(22) Zhou, L.; Lv, W.; Bai, L.; Han, Y.; Wang, J.; Shi, W.; Huang, G. CFD-DEM study of gas-solid flow characteristics in a fluidized bed with different diameter of coarse particles. *Energy Reports* **2022**, *8*, 2376−2388.

(23) Chen, X.; Zhong, W.; Heindel, T. J. Fluidization of cylinder particles in a fluidized bed. *Advanced Powder Technology* **2017**, *28* (3), 820−835.

(24) Tang, T.; He, Y.; Tai, T.; Wen, D. DEM numerical investigation of wet particle flow behaviors in multiple-spout fluidized beds. *Chem. Eng. Sci.* **2017**, *172*, 79−99.

(25) Zhang, Y.; Li, Y.; Gao, Z.; Li, G.; Zhao, Y.; Duan, C.; Dong, L. Effects of drag force correlations on the mixing and segregation of polydisperse gas-solid fluidized bed by CFD-DEM simulation. *Canadian Journal of Chemical Engineering* **2019**, *97* (S1), 1708−1717.

(26) Fu, L.; Bai, H.; Bai, D.; Xu, G. Hydrodynamics of gas-solid fluidization at ultra-high temperatures. *Powder Technol.* **2022**, *406*, 117552.

(27) Xu, H.; Wang, W.; Zhong, W.; Ma, C.; Zhang, H. Experimental study of fluidization characteristics of Geldart-D particles in pressurized bubbling fluidized bed. *Advanced Powder Technology* **2022**, *33* (3), 103453.

(28) Wang, Z.; Saidi, M.; Lim, C. J.; Grace, J. R.; Basirat Tabrizi, H.; Chen, Z.; Li, Y. Comparison of DEM simulation and experiments in a dual-column slot-rectangular spouted bed with a suspended partition. *Chemical Engineering Journal* **2016**, *290*, 63−73.

(29) Ma, H.; Xu, L.; Zhao, Y. CFD-DEM simulation of fluidization of rod-like particles in a fluidized bed. *Powder Technol.* **2017**, *314*, 355−366.

(30) Drew, D. A. Mathematical modeling of two-phase flow. *Annu. Rev. Fluid Mech.* **1983**, *15* (1), 261−291.

(31) Cao, W.; Jia, Z.; Zhao, Z.; Zhou, L. Validation and simulation of cavitation flow in a centrifugal pump by filter-based turbulence model. *Engineering Applications of Computational Fluid Mechanics* **2022**, *16* (1), 1724−1738.

(32) ESSS-Rocky. *Rocky-dem technical manual*; Engineering Simulation and Scientific Software, 2018, https://rocky.esss.co/technical-library/.

(33) Hou, Q.; E, D.; Kuang, S.; Yu, A. A process scaling approach for CFD-DEM modelling of thermochemical behaviours in moving bed reactors. *Fuel Process. Technol.* **2020**, *202*, 106369.

(34) Hu, J.; Xu, G.; Shi, Y.; Huang, S. The influence of the blade tip shape on brownout by an approach based on computational fluid dynamics. *Engineering Applications of Computational Fluid Mechanics* **2021**, *15* (1), 692−711.

(35) Norouzi, H. R.; Zarghami, R.; Sotudeh-Gharebagh, R.; Mostoufi, N. *Coupled CFD-DEM modeling: formulation, implementation and application to multiphase flows*. John Wiley & Sons, 2016.

(36) Wu, W.; Duan, L.; Li, L.; Liu, D. Investigation on a single char particle movement behavior in a bubbling fluidized bed under high temperature. *Fuel Process. Technol.* **2022**, *236*, 107412.

(37) Peng, Z. B.; Doroodchi, E.; Luo, C. M.; Moghtaderi, B. Influence of void fraction calculation on fidelity of CFD-DEM simulation of gas-solid bubbling fluidized beds. *Aiche Journal* **2014**, *60* (6), 2000−2018.

(38) Wang, S.; Luo, K.; Yang, S.; Hu, C.; Fan, J. Parallel LES-DEM simulation of dense flows in fluidized beds. *Applied Thermal Engineering* **2017**, *111*, 1523−1535.

(39) Chen, J.; Zhong, S.; Li, D.; Zhao, C.; Han, C.; Yu, G.; Song, M. Effect of the blend ratio on the co-gasification of biomass and coal in a bubbling fluidized bed with CFD-DEM. *Int. J. Hydrogen Energy* **2022**, *47* (53), 22328−22339.

(40) Han, C.; Bai, L.; Zhou, C.; Sun, W.; Zhou, L. CFD-DEM simulation and experimental study of flow pattern transition in a rectangular spouted bed. *Powder Technol.* **2022**, *399*, 117179.

(41) Lacey, P. M. C. Developments in the theory of particle mixing. *Journal of applied chemistry* **1954**, *4* (5), 257−268.